02 May 2013, 2:00 pm - 3:30 pm

Comparison Between Dynamic Responses of Hollow and Solid Piles for Offshore Wind Turbine Foundations

M. Bayat
Aalborg University, Denmark

Lars Vabbersgaard Andersen
Aalborg University, Denmark

Lars Bo Ibsen
Aalborg University, Denmark

Commemorate the Legacy of Ralph B. Peck
April 29 - May 4, 2013 CHICAGO
Seventh International Conference on
Case Histories in Geotechnical Engineering
and Symposium in Honor of Clyde Baker

COMPARISON BETWEEN DYNAMIC RESPONSES OF HOLLOW AND SOLID PILES FOR OFFSHORE WIND TURBINE FOUNDATIONS

M. Bayat
Dept. of Civil Eng., Aalborg University
Aalborg, Denmark

L. V. Andersen, L. B. Ibsen
Dept. of Civil Eng., Aalborg University
Aalborg, Denmark

ABSTRACT

The offshore wind energy industry is turning out ever larger numbers of offshore wind turbines every year. One way to achieve a cost-effective design is to have a better understanding of the dynamic response of offshore structures. That is why it is getting more and more important to understand the dynamic behavior of soil and interaction between soil and piles. To avert damage to offshore foundation, it becomes necessary to identify and quantify the soil-structure interaction and the related damping effects on the system. In this study, a single pile is investigated by means of boundary integral equations. The pile is modeled as a solid or hollow cylinder and the dynamic excitation is applied vertically. The surface along the entire interface is considered rough and with full contact between the soil and the structure. Somigliana's identity, Betti's reciprocal theorem and Green's function are employed to derive the dynamic stiffness of pile, assuming that the soil is a linear viscoelastic medium. The dynamic stiffness is compared for solid and hollow cylinders by considering different values of material properties including the material damping. Modes of resonance and anti-resonance are identified and presented. It is observed that the absolute value of normalized dynamic stiffness is independent of Young's modulus and Poisson's ratio, whereas it is dependent on the soil's damping.

INTRODUCTION

There are more than 7,000 offshore structures around the world. Structures to support wind turbines come in various shapes and sizes; the most common are Monopile, Jacket, Tripod, Gravity base and Floating structures (see Fig. 1). Based on dimensions of pile it can be solid and hollow cylinder. The tendency of large-size offshore wind turbines have increased during the last 10 years. As wind turbines get larger and are located in deeper water, jacket structures are expected to become more attractive. Generally, a fixed platform is described as consisting of two main components; the substructure and the superstructure. Superstructure or 'topsides' is supported on a deck, which is mounted on the jacket structure. Substructure is either a tubular or solid cylinder.

Support structures for offshore wind turbines are highly dynamic, having to cope with combined wind and hydrodynamic loading and complex dynamic behavior from the wind turbine. The offshore jacket platform is a complex and nonlinear system, which can be excited with harmful vibration by the external loads. It is vital to capture the integrated effect of the total loads. However, the total loading can be significantly less than the sum of the constituent loads. This is because the loads are not coincident, and because of the existence of different kinds of damping such as aerodynamic and soil damping which damps the motions due to the different loads. The dynamic stiffness indicates the stability and resonance behavior. In fact, the overall weight of the modern wind turbines is minimized, which makes it more flexible and corollary more secretive to low frequency dynamic. Another side, wave propagation in elastic and viscoelastic medium are considerable issues especially when there is an earthquake. In modern offshore wind turbines, instabilities or stability occur due to the coupled damping of the upper side of the wind turbine and the lower part of that as the foundation. Most of the failure phenomena are caused by fatigue while the first natural frequency plays an important role. In this aspect, stiffness has a predominant role to evaluate the first natural frequency. The first estimation for stiffness of foundation comes through the analysis of soil-structure interaction. Applying inaccurate algorithms in the soil-structure media may also occur when two different numerical methods are coupled, e.g. the boundary element method (BEM) and the finite element method (FEM); this problem

may become even more serious when coupled algorithms and different physical media are considered simultaneously in the same analysis as it was mentioned by Jr and Mansur [2006]. Soil-structure interaction (SSI) can be analyzed based on two methods namely substructure and direct methods which are highlighted by Wolf [1985]. Maheshwari and Khatri [2011] analyzed a SSI for a combined footing and supporting column on soft soil by using an iterative Gauss Elimination technique while the footing was modeled as a beam having finite flexural rigidity. Srisupattarawanit et al. [2006] applied BEM and a computation method to compute nonlinear random finite depth waves in order to be coupled with an elastic structure. Guenfoud et al. [2009] employed Green's function to solve the integrals resulting from Lamb's problem in order to study the interaction between soil and structures subjected to a seismic load. Padron et al. [2009] studied the SSI between nearby pile supported structures in a viscoelastic half-space by using BEM-FEM in the frequency domain. Genes [2012] applied a parallelized coupled model based on BEM-FEM to analyze the SSI for arbitrarily shaped, large-scale SSI problems and validation was shown. Comprehensive reviews in applying different methods pertain to SSI have been done by Mpahmoudpour et al. [2011].

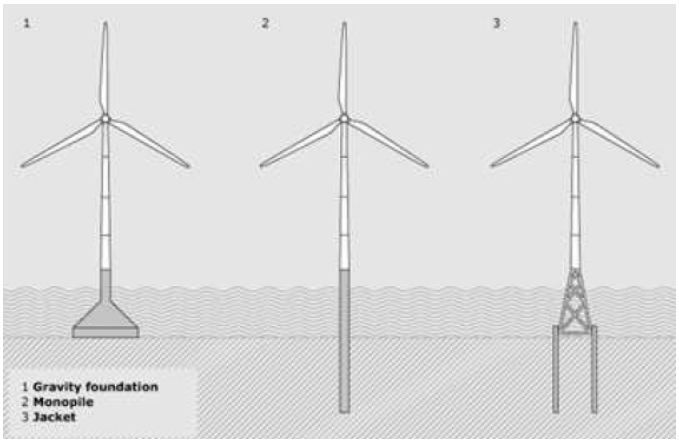

Fig. 1. Different types of offshore wind foundation.

Zienkiewicz [1982] developed the FEM discretization to present the behavior of various classes of soil and rock. He presented a concrete as two-phase medium composed of a solid skeleton and an interstitial fluid. Karim et al. [2002] analyzed the saturated porous elastic soil layer under cyclic loading by using a two-dimensional mesh free Galerkin method by having periodic conditions. A meshless method was an effective alternative, because it is difficult for FEM to analyze the problems associated with the moving boundary. The time domain response of a jacket offshore tower while the soil resistance to the pile movement was modeled using p–y and t–z curves to account the soil nonlinearity and energy dissipation, was presented by Mostafa and Naggar [2004] by employing a FE package in order to do parameters study. Andersen and Nielsen [2003] applied FEM with transmitting boundary element and presented a solution in the frequency domain of an elastic half-space to a moving force on its surface. And also, a two- and three-dimensional combined FEM and BEM have been carried out for two railway tunnel structures in order to investigate what reliable information can be gained from a two-dimensional model to aid a tunnel design process or an environmental vibration prediction based on 'correcting' measured data from another tunnel in similar ground in research by Andersen and Jones [2003]. Then the steps in the FEM and BEM formulations were discussed, and the problems in describing material dissipation in the moving reference frame investigated by Andersen et al. [2007]. Badia et al. [2009] applied FEM to simulate the interaction between a fluid and a poroelastic structure due to the fact that both subproblems are indefinite. Andersen et al. [2012] used numerical method to analyze a nonlinear stochastic p–y curve for calculating the monopile response. The time-domain results for soil-foundation-structure interaction by considering the dependence of the foundation on the frequency of excitation were presented by Cazzania and Ruge [2012] by using FEM. Also, due to the unbounded nature of a soil medium, the computational size of these methods is very large. For this reason, it is important to establish some simple mathematical models which reduce the computational cost of analysis as well as increase the accuracy of results.

There are several analytical solutions for this type of problem. Peng and Yu [2011] obtained the analytical solutions of the torsional impedance saturated soil by using transfer matrix method. The effects of important parameters such as frequency and the rigidity ratio of different soil layers at the top of the pile were analyzed. Belotserkovets and Prevost [2011] developed a full-analytical method and an exact unique solution of the coupled thermo/hydro/mechanical response of a fluid saturated porous sphere subject to a pressure stress pulse on the outer boundary. The method of solution was based on the Laplace transformation method. Prakash and Puri [2006] presented methods for determining the dynamic response of machine foundations subjected to harmonic load. The soil stiffness was considered frequency independent for design of machine foundations. Li and Zhang [2010] presented an analytical solution in frequency domain by means of a variable separating method and then a semi-analytical solution was obtained using an numerical convolution method. Chai et al. [2011] employed the thin layer stiffness method, the matrix stiffness of the thin layer for P–SV and analytical expressions for the effective phase velocity of the surface waves to illustrate the effects of the body waves on the observed phase velocity through the phase analysis of the vibrations of both the surface waves and the body waves.

It may be noted that existing literature on offshore monopile foundations as cited above have been solved experimentally or theoretically based on numerical and analytical methods. To the best of our knowledge, no work has been reported till date that analyzes offshore foundation as long hollow and solid cylinders by using appropriate mathematical approach and employing the Green's function and integral method. This study attempts to concentrate on this investigation. In this paper, offshore foundations in an elastic and viscoelastic

media are investigated by modeling that as long tabular and solid piles. The integral method along with the Betti's reciprocal theorem, Somigliana's identity and Green's function are employed. The vertical loads are applied on the surface along the entire interface by considering rough and full contact between the soil and structure. The effect of material properties such as Young's modulus and Poisson's ratio on dynamic stiffness and phase angle are illustrated. This work aims to investigate the effect of some basic factors such as geometry, damping and frequency on stiffness, phase velocity in a pile. The exact solutions are obtained in elastic and frequency domain. Modes of resonance and anti-resonance are identified and presented.

GENERAL DEFINITION OF MODEL

Consider a thin axisymmetric circular cylinder with small wall thickness and radius R, as shown in Fig. 2. This cylinder is subject to harmonically varying forced displacement with the cyclic frequency ω and applied in the x_3 direction, along the center axis of the cylinder. In this case, pure antiplane shear wave propagation (SH-waves) occur which means that there is no displacement in the x_1 or x_2 directions. Axial symmetry in geometry and loading is assumed and cylindrical coordinates are considered.

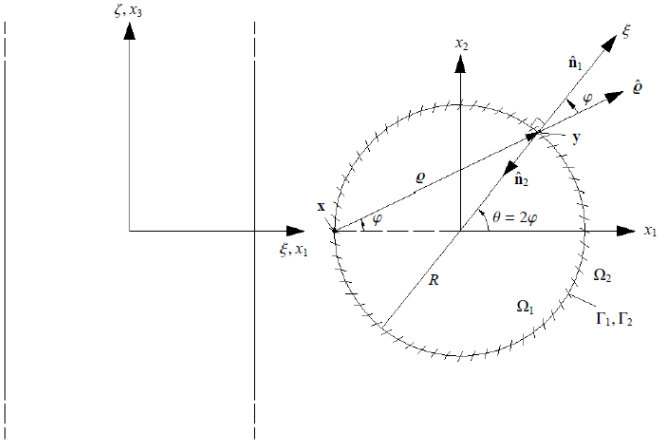

Fig. 2.Cross section of tubular offshore wind turbine foundation.

THEORETICAL FORMULATION AND EQUILIBRIUM EQUATIONS

Somigliana's identity is based on the dynamic reciprocity theorem and the fundamental solution which is used for wave propagation in elastic media. The three-dimensional frequency-domain version of Somigliana's identity reads:

$$C(\boldsymbol{x}) \cup_i (\boldsymbol{x},\omega) + \int_\Gamma P^*_{il}(\boldsymbol{x},\omega;\boldsymbol{y}) \cup_l (\boldsymbol{y},\omega) d\Gamma(\boldsymbol{y}) = \int_\Gamma \cup^*_{il} (\boldsymbol{x},\omega;\boldsymbol{y}) P_l(\boldsymbol{y},\omega) d\Gamma(\boldsymbol{y}) + \int_\Omega \cup^*_{il} (\boldsymbol{x},\omega;\boldsymbol{y})\, \rho B_l(\boldsymbol{y},\omega) d\Omega(\boldsymbol{y}) \quad (1)$$

where

$$\cup^*_{il} (\boldsymbol{x},\omega;\boldsymbol{y}) = \int_{-\infty}^{\infty} u^*_{il}(\boldsymbol{x},t;\boldsymbol{y},0) e^{-i\omega t} dt \quad (2a)$$

$$P^*_{il}(\boldsymbol{x},\omega;\boldsymbol{y}) = \int_{-\infty}^{\infty} p^*_{il}(\boldsymbol{x},t;\boldsymbol{y},0) e^{-i\omega t} dt \quad (2b)$$

$C(\boldsymbol{x})$ is a coefficient dependent a the position $(\boldsymbol{x})$. In particular, for any interior point within the domain Ω, the constant takes the value $C(\boldsymbol{x}) = 1$. Actually, the value of $C(\boldsymbol{x})$ simply corresponds to the part of the point that is included in the domain Γ. Hence, $C(\boldsymbol{x}) = 0$ at an exterior point, and $C(\boldsymbol{x}) = 1/2$ for a point on a smooth part of the boundary Γ. A detailed derivation for a smooth part of a surface can be found in the work by Dominguez [1993].

And also, by assuming the surface and body quantities in the physical state vary harmonically with at the circular frequency ω, then:

$$u_l(\boldsymbol{x},t) = \cup_l (\boldsymbol{x},\omega) e^{-i\omega t},\ p_l(\boldsymbol{x},t) = P_l(\boldsymbol{x},\omega) e^{-i\omega t},\ b_l(\boldsymbol{x},t) = B_l(\boldsymbol{x},\omega) e^{-i\omega t} \quad (3)$$

where $u_l(\boldsymbol{x},t)$ are the components of the displacement field, $p_l(\boldsymbol{x},t)$ is the surface traction and $b_l(\boldsymbol{x},t)$ is the load per unit mass in coordinate direction i. Vector $\boldsymbol{x}$ is the position in space and t is the time. Furthermore, based on Caushy's law the relation between surface traction and the Caushy stress (σ_{ij}) tensor is: $p_i(\boldsymbol{x},t) = \sigma_{ij}(\boldsymbol{x},\omega) n_j(\boldsymbol{x})$.

$\cup^*_{il}(\boldsymbol{x},\omega;\boldsymbol{y})$ and $P^*_{il}(\boldsymbol{x},\omega;\boldsymbol{y})$ are the Green's functions for the displacements and the surface traction in the frequency domain or, in other words, they are the Fourier transforms of $u^*_{il}(\boldsymbol{x},t;\boldsymbol{y},0)$ and $p^*_{il}(\boldsymbol{x},t;\boldsymbol{y},0)$, respectively. It can be mentioned here that the Green's function for a vector field is a second-order tensor with the components $g_{il}(\boldsymbol{x},t;\boldsymbol{y},\tau)$ which provide the response at the point $\boldsymbol{x}$ and time t in coordinate direction i due to a unit magnitude concentrated force acting at the point $\boldsymbol{y}$ and time τ in coordinate direction l. Hence, whereas the displacement field $\mathbf{u}(\boldsymbol{x},t)$ is a vector field with the components $u_i(\boldsymbol{x},t)$, the corresponding Green's function is a tensor field $\mathbf{u}^*(\boldsymbol{x},t;\boldsymbol{y},\tau)$ with the doubly indexed components $u^*_{il}(\boldsymbol{x},t;\boldsymbol{y},\tau)$.

FREQUENCY- DOMAIN EQUATION OF MOTION FOR SH-WAVES

The antiplane shear assumption induces the displacement components u_1 and u_2 which are identically equal to zero and partially derivatives with respect to x_3 vanish, only the displacement component u_3 in the direction out of the (x_1, x_2) plane exists and it is constant in along the x_3 direction. In the case of elastodynamics, this corresponds to the propagation of SH-waves in the (x_1, x_2) plane. When antiplane shear is considered, only the third component of the displacement field is different from zero. This holds for both the physical field and the Green's function. Hence, Somigliana's identity simplifies to a scalar integral equation as:

$$C(\boldsymbol{x}) \cup_3 (\boldsymbol{x},\omega) + \int_\Gamma P^*_{33}(\boldsymbol{x},\omega;\boldsymbol{y}) \cup_3 (\boldsymbol{y},\omega) d\Gamma(\boldsymbol{y}) = \int_\Gamma \cup^*_{33} (\boldsymbol{x},\omega;\boldsymbol{y}) P_3(\boldsymbol{y},\omega) d\Gamma(\boldsymbol{y}) +$$

$\int_{\Omega} \cup_{33}^{*} (\boldsymbol{x}, \omega; \boldsymbol{y})\, \rho B_3(\boldsymbol{y}, \omega) d\Omega\,(\boldsymbol{y})$ (4)

SOLUTION FOR A HOLLOW CYLINDER

By considering smooth interfaces, Somigliana's identity (4) for the two domains Ω_1 and Ω_2 o(as shown in Fig. 2) reduces to:

$$\frac{1}{2} \cup_3^{(1)} (\boldsymbol{x}, \omega) + \int_{\Gamma_1} P_{33}^{*}(\boldsymbol{x}, \omega; \boldsymbol{y}) \cup_3^{(1)} (\boldsymbol{y}, \omega) d\Gamma\,(\boldsymbol{y}) = \int_{\Gamma_1} \cup_{33}^{*} (\boldsymbol{x}, \omega; \boldsymbol{y}) P_3^{(1)}(\boldsymbol{y}, \omega) d\Gamma\,(\boldsymbol{y}) \quad (5)$$

$$\frac{1}{2} \cup_3^{(2)} (\boldsymbol{x}, \omega) + \int_{\Gamma_2} P_{33}^{*}(\boldsymbol{x}, \omega; \boldsymbol{y}) \cup_3^{(2)} (\boldsymbol{y}, \omega) d\Gamma\,(\boldsymbol{y}) = \int_{\Gamma_2} \cup_{33}^{*} (\boldsymbol{x}, \omega; \boldsymbol{y}) P_3^{(2)}(\boldsymbol{y}, \omega) d\Gamma\,(\boldsymbol{y}) \quad (6)$$

where $\cup_3^{(1)} (\boldsymbol{x}, \omega)$ and $\cup_3^{(2)} (\boldsymbol{x}, \omega)$ are the displacements in the x_3-direction along the boundaries Γ_1 and Γ_2, respectively, whereas $P_3^{(1)}(\boldsymbol{y}, \omega)$ and $P_3^{(2)}(\boldsymbol{y}, \omega)$ are the corresponding surface tractions.

Green's function

The fundamental solution for the antiplane displacements is (Domínguez [1993]):

$$\cup_{33}^{*} (\boldsymbol{x}, \omega; \boldsymbol{y}) = \frac{1}{2\pi\mu} K_0(\mathrm{i} k_s \varrho),\ \varrho = |\boldsymbol{x} - \boldsymbol{y}|,\ \mathrm{i} = \sqrt{-1} \quad (7)$$

where, μ is the shear modulus, K_m represents the modified Bessel function of the second kind and order m and k_s is the wavenumber. The relation between wavenumber and phase speed c_s is:

$$k_s = \frac{\omega}{c_s}$$

where $c_s$is dependent on the material properties, and it is defined as:

$$\begin{cases} For\ hysteretic\ material\ damping: c_s^2 = (1 + \mathrm{i}\eta)\frac{\mu}{\rho} \\ For\ materials\ without\ damping: \quad c_s^2 = \frac{\mu}{\rho} \end{cases} \quad (9)$$

where η is the loss factor and ρ is the material density. For a homogeneous isotropic linear elastic material, the generalized Hooke's law forming the relation between stresses, $\sigma_{ij}(\boldsymbol{x}, t)$, and strains, $\epsilon_{ij}(\boldsymbol{x}, t)$, simplifies to

$$\sigma_{ij}(\boldsymbol{x}, t) = \lambda\, \Delta(\boldsymbol{x}, t)\delta_{ij} + 2\mu\, \epsilon_{ij}(\boldsymbol{x}, t) \quad (10)$$

where λ and μ are the Lame constants, δ_{ij} is Kronecker delta and $\Delta(\boldsymbol{x}, t) = \epsilon_{kk}(\boldsymbol{x}, t)$ is the dilation. Substituting the fundamental displacements $\cup_{33}^{*} (\boldsymbol{x}, \omega; \boldsymbol{y})$ from Eq. 7 into Hooke's law (Eq. 10) and applying Caushy's stress law the fundamental surface shear stresses is obtained:

$$P_{33}^{*}(\boldsymbol{x}, \omega; \boldsymbol{y}) = -\frac{\mathrm{i} k_s}{2\pi} \frac{\partial \varrho}{\partial n} K_0(\mathrm{i} k_s \varrho), k_s = \sqrt{\frac{\omega^2 \rho}{\mu}} \quad (11)$$

$\frac{\partial \varrho}{\partial n}$ defines the partial derivative of the distance ϱ between the source and observation points, $\boldsymbol{x}$ and $\boldsymbol{y}$, in the direction of the outward normal:

$$\frac{\partial \boldsymbol{\varrho}}{\partial n} = \begin{cases} \hat{\boldsymbol{\varrho}}(\boldsymbol{x}, \boldsymbol{y}) \cdot \hat{\boldsymbol{n}}(\boldsymbol{y}) = \cos(\varphi) & for\ \boldsymbol{x} \in \Gamma_1 \\ -\hat{\boldsymbol{\varrho}}(\boldsymbol{x}, \boldsymbol{y}) \cdot \hat{\boldsymbol{n}}(\boldsymbol{y}) = -\cos(\varphi) & for\ \boldsymbol{x} \in \Gamma_1 \end{cases} \quad (12a)$$

where

$$\hat{\varrho}(\boldsymbol{x}, \boldsymbol{y}) = \frac{\boldsymbol{x} - \boldsymbol{y}}{|\boldsymbol{x} - \boldsymbol{y}|} \quad (12b)$$

Here φ is the angle between the distance vector $\varrho = \varrho\hat{\varrho}$ and the normal vector $\hat{n}$.

Continuity conditions

The continuity conditions for the displacements across the interface for the forced displacement with constant amplitude $\hat{U}_3$and in phase along the cylindrical interface, $\Gamma \equiv \Gamma_1$, provides the result:

$$\cup_3^{(1)} (\boldsymbol{x}, \omega) = \cup_3^{(2)} (\boldsymbol{x}, \omega) = \hat{U}_3\,(\omega), \boldsymbol{x} \in \Gamma \quad (13a)$$

$$P_3^{(1)}(\boldsymbol{y}, \omega) = \hat{P}_3^{(1)}(\omega)\,, \boldsymbol{x} \in \Gamma \quad (13b)$$

$$P_3^{(2)}(\boldsymbol{y}, \omega) = \hat{P}_3^{(2)}(\omega)\,, \boldsymbol{x} \in \Gamma \quad (13c)$$

Substituting the continuity conditions (Eq. (13)) into Eqs. 5 and 6, by having the constant amplitude for the forced displacement yield a set of linear integral equations:

$$\hat{U}_3\,(\omega) \left(\frac{1}{2} + \int_{\Gamma} P_{33}^{*}(\boldsymbol{x}, \omega; \boldsymbol{y}) d\Gamma\,(\boldsymbol{y})\right) = \hat{P}_3^{(1)}(\omega) \int_{\Gamma} \cup_{33}^{*} (\boldsymbol{x}, \omega; \boldsymbol{y}) d\Gamma\,(\boldsymbol{y}) \quad (14)$$

$$\hat{U}_3\,(\omega) \left(\frac{1}{2} - \int_{\Gamma} P_{33}^{*}(\boldsymbol{x}, \omega; \boldsymbol{y}) d\Gamma\,(\boldsymbol{y})\right) = \hat{P}_3^{(2)}(\omega) \int_{\Gamma} \cup_{33}^{*} (\boldsymbol{x}, \omega; \boldsymbol{y}) d\Gamma\,(\boldsymbol{y}) \quad (15)$$

Analysis

According to the frequency-domain equation of motion for each domain, inside and outside of the hollow cylinder, the dynamic stiffness can be obtained. Eliminating $P_{33}^{*}(\boldsymbol{x}, \omega; \boldsymbol{y})$ from equations 14 and 15, the constant amplitude can be written in terms of the traction on the interface, as follows:

$$\hat{U}_3\,(\omega) = 2\hat{P}_3(\omega) \int_{\Gamma} \cup_3^{*} (\boldsymbol{x}, \omega; \boldsymbol{y}) d\Gamma\,(\boldsymbol{y}) \quad (16)$$

where the mean traction on either side of the interface ($\hat{P}_3(\omega)$) is:

$$\hat{P}_3(\omega) = \frac{1}{2}(\hat{P}_3^{(1)}(\omega) + \hat{P}_3^{(2)}(\omega)) \quad (17)$$

The general dynamic stiffness ($S_{33}(\omega)$) per unit surface of the interface related to displacement along the cylinder axis for arbitrary geometry of the infinite cylinder becomes:

$$S_{33}(\omega) = 2L_{\Gamma} \frac{\hat{P}_3(\omega)}{\hat{U}_3(\omega)} = \frac{L_{\Gamma}}{\alpha}, \alpha = \frac{1}{2}\frac{\hat{U}_3(\omega)}{\hat{P}_3(\omega)} = \int_{\Gamma} \cup_3^{*} (\boldsymbol{x}, \omega; \boldsymbol{y}) d\Gamma\,(\boldsymbol{y})$$

(18)

where L_Γ is the length of the interface Γ, measured in the (x_1, x_2) plane. In the presented case, an offshore foundation is considered as an infinite circular cylinder with the radius R that is with $L_\Gamma = 2\pi R$. In order to compute α, the cylindrical polar coordinates $\alpha(\xi, \theta, \zeta)$ are introduced (see Fig. 2) such that:

$$x_1 = \xi\cos(\theta), x_2 = \xi\sin(\theta), x_3 = \zeta \quad (19)$$

In these coordinates, the boundary Γ is defined by $\xi = R,\ 0 \leq \theta < 2\pi, \infty < \zeta < \infty$.

In particular, when an observation point $\boldsymbol{x}$ with the plane coordinates $(x_1, x_2 = (-1,0)$ is considered (see Fig. 2), the distance ϱ between the source and observation point becomes:

$$\varrho = R\frac{sin2\varphi}{sin\varphi} = 2Rcos\ \varphi \quad (20)$$

Making use of the fact that $\theta = 2\varphi$, Eq. 16 may then be evaluated as:

$$\alpha = \frac{1}{2\pi\mu}\int_0^{2\pi} K_0(\mathrm{i}k_s\varrho)Rd\theta = \frac{R}{\pi\mu}\int_0^{\pi} K_0(2\mathrm{i}k_sRcos\varphi)d\varphi = \frac{R}{\mu}\boldsymbol{J}_0(k_sR)K_0(\mathrm{i}k_sR) \quad (21)$$

Here, $\boldsymbol{J}_0$ is the Bessel function of the first kind and order 0. It is noted that $K_0(\mathrm{i}k_sR) \to \infty$ for $k_s \to \infty$. Hence, $S_{33}(\omega) \to 0$ $\omega \to 0$. Furthermore, $\boldsymbol{J}_0(k_sR)$has a number of zeros for $\eta = 0$ and $k_s > 0$. At the corresponding frequencies, $S_{33}(\omega)$ becomes singular.

SOLUTION FOR A SOLID CYLINDER

Based on Somigliana's identity for smooth surface of the rigid cylinder as mentioned above, one domain would be considered for the solid cylinder. By representing the equation of motion for one domain:

$$\frac{1}{2}\cup_{s3}^{(2)}(\boldsymbol{x},\omega) + \int_{\Gamma_2} P_{33}^*(\boldsymbol{x},\omega;\boldsymbol{y})\cup_{s3}^{(2)}(\boldsymbol{y},\omega)d\Gamma(\boldsymbol{y}) = \int_{\Gamma_2}\cup_{33}^*(\boldsymbol{x},\omega;\boldsymbol{y})P_{s3}^{(2)}(\boldsymbol{y},\omega)d\Gamma(\boldsymbol{y}) \quad (22)$$

Considering a constant amplitude for the forced displacement and in phase along the cylindrical interface provides the result as:

$$\hat{\cup}_{s3}(\omega)\left(\frac{1}{2} - \int_\Gamma P_{33}^*(\boldsymbol{x},\omega;\boldsymbol{y})d\Gamma(\boldsymbol{y})\right) = \hat{P}_{s3}^{(2)}(\omega)\int_\Gamma\cup_{33}^*(\boldsymbol{x},\omega;\boldsymbol{y})d\Gamma(\boldsymbol{y}) \quad (23)$$

The general dynamic stiffness $S_{33}(\omega)$ per unit length along the cylinder of the infinite cylinder becomes:

$$S_{s33}(\omega) = 2L_\Gamma\frac{\hat{P}_{s3}(\omega)}{\hat{\cup}_3(\omega)} = \frac{L_\Gamma}{\alpha_s}, \alpha_s = \frac{1}{2}\frac{\hat{\cup}_{s3}(\omega)}{\hat{P}_3(\omega)} = \frac{\int_\Gamma\cup_3^*(\boldsymbol{x},\omega;\boldsymbol{y})d\Gamma(\boldsymbol{y})}{\left(\frac{1}{2} - \int_\Gamma P_{33}^*(\boldsymbol{x},\omega;\boldsymbol{y})d\Gamma(\boldsymbol{y})\right)} \quad (24)$$

by substituting the relation for fundamental surface shear stress, the dynamic stiffness can be written as:

$$S_{s33}(\omega) = \frac{L_\Gamma}{\alpha_s} = \frac{2\pi R}{\alpha_s}, \alpha_s = \frac{1}{2}\frac{\hat{\cup}_{s3}(\omega)}{\hat{P}_3(\omega)} = \frac{\frac{R}{\pi\mu}\int_0^{\pi} K_0(2\mathrm{i}k_sRcos\varphi)d\varphi}{\left(\frac{1}{2} + \int_0^{\pi}\frac{Rik_s}{\pi\mu}K_1(2\mathrm{i}k_sRcos\varphi)d\varphi\right)} \quad (25)$$

Then

$$\alpha_s = \frac{\frac{R}{\pi\mu}\int_0^{\pi} K_0(2\mathrm{i}k_sRcos\varphi)d\varphi}{\left(\frac{1}{2} + \frac{R}{\pi}\int_0^{\pi}\mathrm{i}k_scos(\varphi)K_1(2\mathrm{i}k_sRcos\varphi)d\varphi\right)}$$

NUMERICAL RESULTS

For numerical illustration of the elastic solutions of this study, a thin long hollow and solid cylinders with mean radius R = 3.0(m) is considered. The material properties are considered as (Liingaard and Andersen [2007]):

Table 1. *Material Properties*

Density ($\frac{kg}{m^3}$)	Young's Modulus ($\frac{N}{m^2}$)	Loss factor
1861	9411×10^3	Between: 0.01~0.1
	13596×10^3	

Results and Discussion for Hollow cylinder

In the following, results are presented in non-dimensional frequency $a_0 = \frac{\omega R}{c_s}$ and the normalized dynamic stiffness $\left|\frac{S_{33}(\omega)}{Z}\right|$, where $Z = 4\pi(1+\mathrm{i}\eta)\mu$. Different values of material properties such as Young's modulus, loss factor and Poisson's ratio are considered.

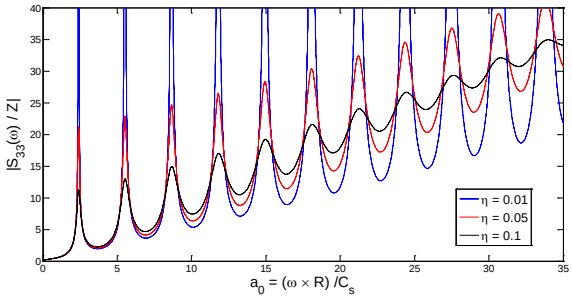

Fig. 3. Normalized dynamic stiffness per unit length of an infinite cylinder due to dynamic vertical load in the axial direction for different values of the loss factor, when $E = 9411 \times 10^3$ *and* $\nu = 0.495$.

Fig. 3 illustrates the normalized dynamic stiffness based on the small deformation theory due to different frequencies of the axial force. The value of stiffness increases with the increase of the load frequency until reaching a peak point then decreases to a local minimum for certain value of frequency

and again increases with the increase of the load frequency to next peak point. This procedure is repeated periodically with the frequency. The local peak point for dynamic stiffness decreases with increasing loss factor, whilst the local minimum point of the stiffness increases with decreasing the loss factor. It can be noticed that the turning point at which the concave curve changes into a convex curve is the same for all different loss factors.

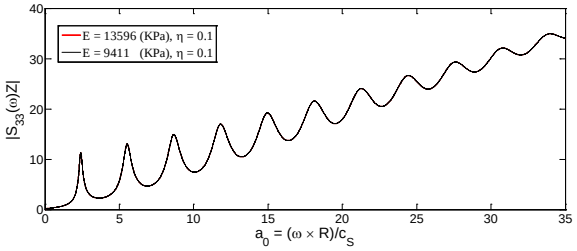

Fig. 4. Normalized dynamic stiffness per unit length of an infinite hollow cylinder due to dynamic vertical load in the axial direction for different values of the Young's modulus $E = 9411 \times 10^3$, $E = 13596 \times 10^3$ *when loss factor* $\eta = 0.1$ *and* $\nu = 0.495$.

Fig. 4 shows the effect of Young's modulus on variation of the dynamic stiffness versus load frequency. The normalized dynamic stiffness has the same value as the soil with lower Young's modulus for all values of load frequency.

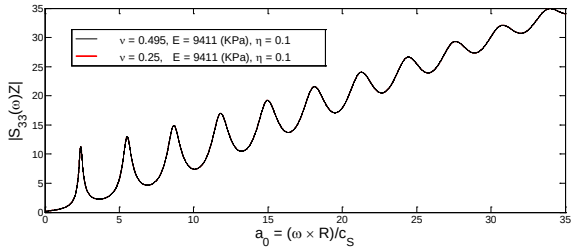

Fig. 5. Normalized dynamic stiffness per unit length of an infinite hollow cylinder due to dynamic vertical load in the axial direction for different values of the Poisson's ratio $\nu = 0.25, \nu = 0.495$ *when loss factor* $\eta = 0.1$ *and* $E = 9411 \times 10^3 N/m^2$

The variation of the dynamic stiffness with load frequency is shown in Fig. 5 for different value of Poisson's ratio. It is observed that the normalized dynamic stiffness is independent from some material properties of soil such as Poisson's ratio and Young's modulus.

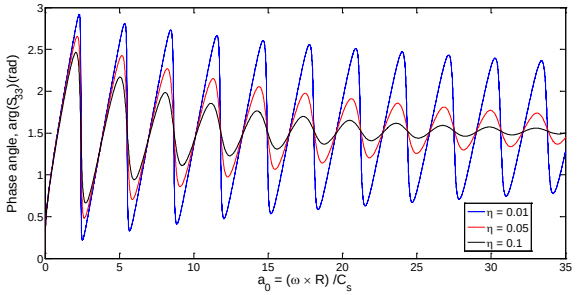

Fig. 6. Phase angle of an infinite hollow cylinder due to dynamic vertical load in the axial direction for different values of the loss factor when the Young's modulus $E = 9411 \times 10^3 \ {}^{N}/_{m^2}$ *and* $\nu = 0.495$.

Fig. 6 compares the phase angle for different values of loss factor versus non-dimensional load frequency. As it is seen, the phase angle oscillating around line $\frac{\pi}{2}$ and the amount of fluctuating around this line decreases with the increase of load frequency. It can be noted that the absolute value of phase angle respect to central line (line $\frac{\pi}{2}$) decreases with the increase of loss factor.

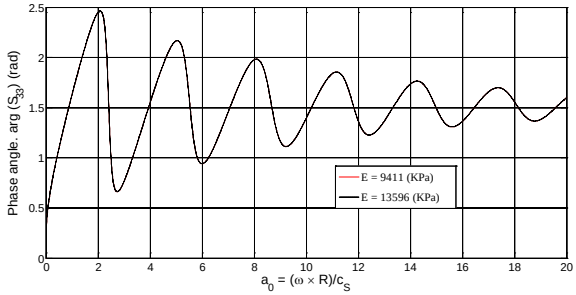

Fig. 7. Phase angle of an infinite hollow cylinder due to dynamic vertical load in the axial direction for different values of the Young's modulus $E = 9411 \times 10^3 N/m^2$ *and* $E = 13596 \times 10^3 N/m^2$ *when loss factor* $\eta = 0.1$ *and* $\nu = 0.495$.

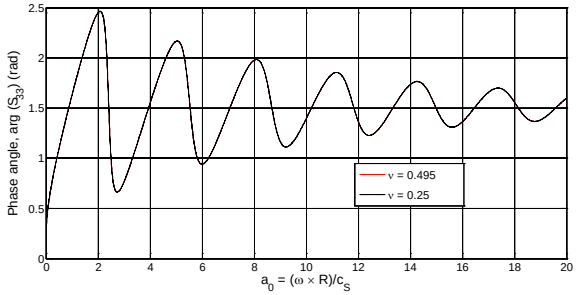

Fig. 8. Phase angle of an infinite hollow cylinder due to dynamic vertical load in the axial direction for different values of the Poisson's ratio $\nu = 0.25$ *and* $\nu = 0.495$ *when* $E = 9411 \times 10^3 N/m^2$ *and the loss factor* $\eta = 0.1$.

Figs. 7 and 8 concern the comparison of phase angle for dynamic stiffness versus non-dimensional load frequency for different values of Young's modulus and Poisson's ratio, respectively. In contrast with the results for different values of loss factor, other material properties such as Young's modulus and Poisson's ratio do not have any effect on phase angle like the results reported in Dominguez [1993], Liingaard, and Andersen [2007].

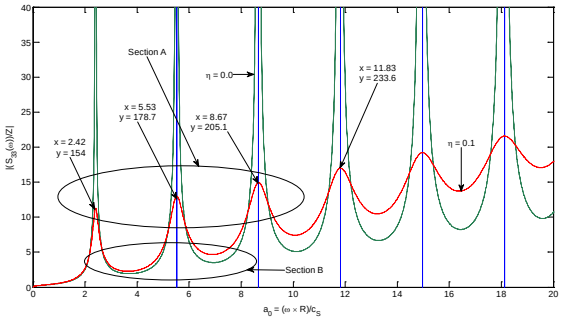

Fig. 9. Normalized dynamic stiffness versus different values of load's frequencies by having different values of loss factor $\eta = 0.0$ *and* $\eta = 0.1$ *when* $\nu = 0.495$ *and* $E = 9411 \times 10^3\ {}^{N}/_{m^2}$.

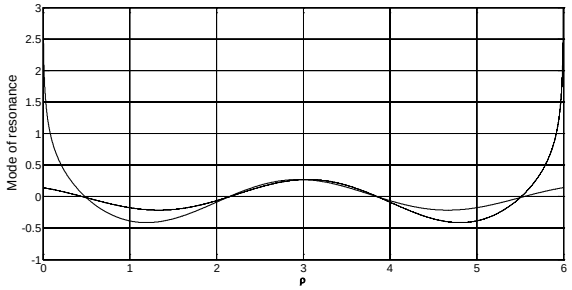

Fig. 10. Scaled mode shape resonance due load with non-dimensional frequency $a_0 = 5.53$ *when loss factor* $\eta = 0.1$ *and* $E = 9411 \times 10^3\ {}^{N}/_{m^2}$.

To present the mode of resonance and anti-resonance, the load frequencies related to minimum and maximum value of the dynamic stiffness are needed. In order to calculate the related frequency, the maximum non-dimensional frequencies for $\eta = 0.1$ is shown in Fig. 9, which is related to section A. For anti-resonance, the frequency related to minimum stiffness in section B as shown in Fig. 9 is needed. Fig. 10 presents the schematic wave mode inside the hollow cylinder versus ϱ ($\varrho = 2Rcos\phi$, from Eq. 20). The value of non-dimensional frequency is taken from section A in Fig. 9, here $a_0 = 5.53$ is considered. Actually, by selecting each value of a_0 to correspond with peak point (such as: $a_0 = 2.42$, (or $a_0 = 5.53$), (or $a_0 = 8.67$), (or $a_0 = 11.83$), the resonance mode can be seen. The continuous line in Fig. 10 represents the wave motion from the left hand side of cylinder to right hand side, and the dash line represents the wave motion from right to left hand side of the hollow cylinder. As seen, the wave motion on left hand side and right hand side have the same sign, both of them are positive which means resonance phenomena. The anti-resonance mode can be seen by selecting the minimum frequencies from section B.

Results and Discussion for Solid cylinder

Figs. 11 and 12 show the effect of loss factor on the dynamic stiffness and the phase angle of the dynamic stiffness versus non-dimensional frequency.

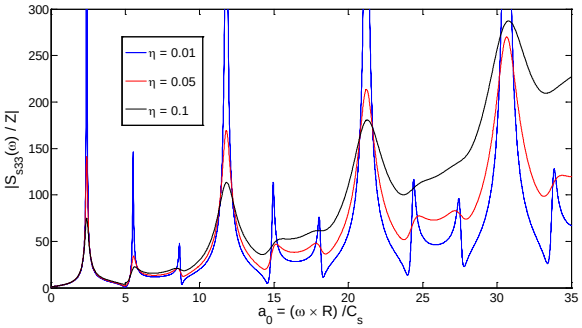

Fig. 11. Non-dimensional dynamic stiffness per unit length of an infinite cylinder due to dynamic vertical load in the axial direction for different values of the loss factor, when $E = 9411 \times 10^3$ *and* $\nu = 0.495$.

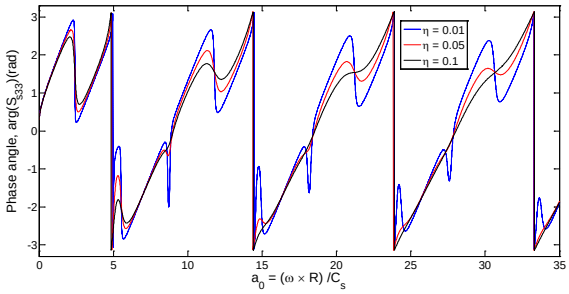

Fig. 12. Phase angle of an infinite solid cylinder due to dynamic vertical load in the axial direction for different values of the loss factor when the Young's modulus $E = 9411 \times 10^3\ {}^{N}/_{m^2}$ *and* $\nu = 0.495$.

As it can be seen form Fig. 11, the rate of increasing the normalized stiffness for smaller value of the loss factor is higher than those for soil with greater value of the loss factor. Moreover, it is seen that by increasing the loss factor the number of local maximum decrease. Fig. 12 shows that at any local maximum of the phase angle, the peaks decrease by increasing the loss factor and the reverse manner happen at local minimum.

Comparison between Hollow and Solid cylinders

In the following figures, results for hollow and solid cylinders versus non-dimensional frequency in presentence of different loss factor, Young's modulus and Poisson's ratio are presented.

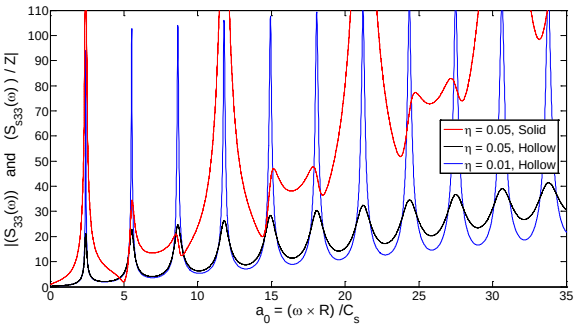

Fig. 13. Comparison between normalized dynamic stiffness

per unit length of an infinite hollow and solid cylinder due to dynamic vertical load for different values of the loss factor versus non-dimensional frequency

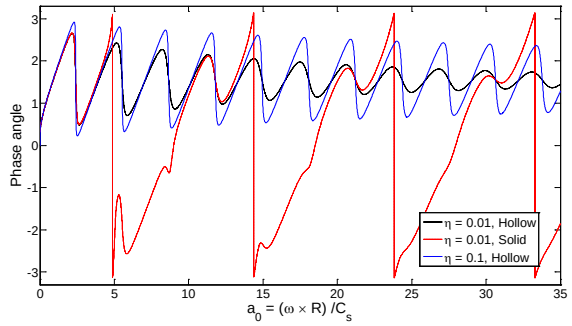

Fig. 14. Comparison between phase angle of an infinite hollow and solid cylinder due to dynamic vertical load for different values of the loss factor versus non-dimensional frequency

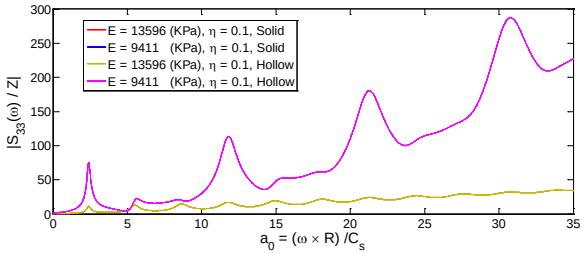

Fig. 15. Comparison between normalized dynamic stiffness per unit length of an infinite hollow and solid cylinder due to dynamic vertical load for different values of the Young's modulus

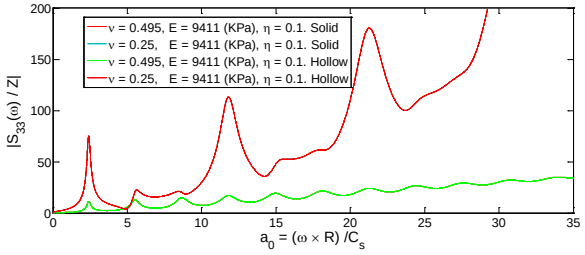

Fig. 16. Comparison between normalized dynamic stiffness per unit length of an infinite hollow and solid cylinder due to dynamic vertical load for different values of the Poisson's ratio

As it is seen from Fig. 13, the numbers of peaks for hollow and solid cylinders are the same. In some peaks, when the frequency is small the stiffness in solid cylinder is greater or smaller than those in hollow cylinder. However for bigger values of frequency ($a_0 > 9$) the stiffness in solid cylinder is greater than hollow cylinder when $\eta = 0.05$. Fig. 14 shows the phase angle in hollow cylinder tends to oscillate around line $\frac{\pi}{2}$ and converges to this line, whilst the behavior of phase angle in solid cylinder in completely different, it is moving periodically without any convergence. It can be seen from Figs. 15 and 16 the stiffness in solid cylinder is greater than those in hollow cylinder by considering the loss factor equal to 0.1.

CONCLUSIONS

Offshore wind turbine foundations are modeled as smooth long hollow and solid cylinders while it is subjected to dynamic vertical excitation. The mathematical approach like boundary integral method is employed to find the exact dynamic stiffness of offshore foundation, phase angle, resonance and anti-resonance mode. The offshore foundation is considered in a viscoelastic media and elastic responses are presented by using the Betti's reciprocal theorem, Somigliana's identity and Green's function. The behavior of the soil with damping and without damping is explored. The effects of material properties such as Young's modulus and Poisson's ratio on dynamic behavior of soil are investigated. The results for the soil with loss factor are validated and compared. Some general observations of this study can be summarized as:

- ✓ The dynamic stiffness increases with the increase of the load frequency until reaching a peak point then decreases to a local minimum for certain value of frequency and again increases with the increase of the load frequency to next peak point for hollow and solid cylinder. This procedure is repeated periodically. The result is similar to hollow cylinder which reported in Liingaard and Andersen [2007].
- ✓ The local peak point of the dynamic stiffness decreases with increasing loss factor in solid and hollow cylinder. The turning point which the concave curve changes into convex curve happens in the same pint for all different loss factors in hollow cylinder while this turning point is not the same for solid cylinders for certain frequency.
- ✓ The Dynamic stiffness and phase angle in a hollow or solid cylinder is independent of the soil's material properties such as Young's modulus and Poisson's ratio whilst it is dependent on loss factor.
- ✓ The phase angle fluctuates around line $\frac{\pi}{2}$ and the amount of fluctuating around this line decreases with the increase of load frequency for hollow cylinder and also by increasing the loss factor it converges to line $\frac{\pi}{2}$, whilst the phase angle does not converge to certain value in solid cylinder.

It is observed that a mathematical approach that pertains to the vertical vibration analysis of foundation provides good understanding about the behavior of soil beside the wave propagation and different modes of the wave. The results reveal that the presented approach gains the physical understanding for offshore foundation in the geo-mechanics field.

REFERENCES

Jr, D.S. and W.J. Mansur [2006], "*Dynamic analysis of fluid-soil-structure interaction problems by the boundary element method*" J. of Comput., No. 219, pp. 498-512.

Wolf, J.P [1985]. "*Dynamic Soil-Structure Interaction*", Prentice-Hall, Englewood Cliffs, NJ.

Maheshwari, P. and S. Khatri [2011]. "*A nonlinear model for footings on granular bed-stone column reinforced earth beds*", Appl. Math. Model., No. 35, pp. 2790-2804.

Srisupattarawanit, T., R. Niekamp and H.G. Matthies [2006], "*Simulation of nonlinear random finite depth waves coupled with an elastic structure*", Comput. Methods Appl. Mech. Engrg., Vol., 195, pp. 3072-3086.

Guenfoud, S., M.N., Amrane, V. Bosakov and N. Ouelaa [2009], "*Semi-analytical evaluation of integral forms associated with Lamb's problem*", Soil Dyn. and Earthquake Engrg., Vol., 29(3), pp. 438-443.

Padron, L.A., J.J. Aznarez and O. Maeso [2009], "*Dynamic structure–soil–structure interaction between nearby piled buildings under seismic excitation by BEM–FEM model*", Soil Dyn. and Earthquake Engrg., Vol. 29(6), pp. 1084-1096.

Genes M.C. [2012]. "*Dynamic analysis of large-scale SSI systems for layered unbounded media via a parallelized coupled finite-element/boundary-element/scaled boundary finite-element model*", Engrg. Anal, with Bound. Elem., Vol. 36(5), pp. 845-857.

Mahmoudpour, S., R. Attarnejad, and C. Behnia [2011], "*Dynamic Analysis of Partially Embedded Structures Considering Soil-Structure Interaction in Time Domain*", Hindawi Publishing Corporation, Math. Prob. in Engrg, Article ID 534968, 23 pages.

Zienkiewicz, O.C. [1982]. "*Basic Formulation of Static and Dynamic Behaviours of Soil and Other Porous Media*", Appl. Math. and Mech., Vol., 3(4), pp. 457-468.

Karim, M.R., T. Nogami and J. G. Wang [2002]. "*Analysis of transient response of saturated porous elastic soil under cyclic loading using element-free Galerkin method "*, Int. J. of Solids and Struct., Vol., 39, pp. 6011- 6033.

Mostafa, Y.E. and M.H. El Naggar [2004]. "*Response of fixed offshore platforms to wave and current loading including soil-structure interaction "*, Soil Dyn. and Earthquake Engrg., Vol., 24(4), pp. 357-368.

Andersen. L and S.R.K. Nielsen [2003], "*Boundary element analysis of the steady state response of an elastic half-space to a moving force on its surface*", Eng. Anal. Bound. Elem., Vol., 27(1), pp. 23-38.

Andersen, L. and C.J.C. Jones [2006], "*Coupled boundary and finite element analysis of vibration from railway tunnels-a comparison of two-and three-dimensional models*", J. Sound Vib., Vol., 293(3), pp 611–25.

Andersen, L., S.R.K. Nielsen and S. Krenk [2007]. "*Numerical methods for analysis of structure and ground vibration from moving loads*", Comput. and Struct., Vol., 85, pp.43-58.

Badia, S., A. Quaini and A, Quarteroni [2009]. "*Coupling Biot and Navier-Stokes equations for modelling fluid-poroelastic media interaction*", MSC, Vol., 65, pp. 1-39.

Andersen, L.V., M.J. Vahdatirad, M.T. Sichani and J.D. Sørensen [2012]. "*Natural frequencies of wind turbines on monopile foundations in clayey soils A probabilistic approach*" Comput. and Geotech., No. 43, pp. 1-11.

Cazzania, A. and P. Ruge [2012]. "*Numerical aspects of coupling strongly frequency-dependent soil–foundation models with structural finite elements in the time-domain*", Soil Dyn. and Earthquake Engrg., Vol., 37, pp. 56-72.

Peng, H and J. Yu [2011]. "*Dynamic Torsional Impedance of Piles in Layered Saturated Soil*", EJGE, Vol., 16, pp. 1147-1161.

Belotserkovets, A and J. H. Prevost [2011]. "*Thermoporoelastic response of a fluid-saturated porous sphere: An analytical solution*", Int. J. of Engrg. Sci., Vol., 16, pp. 3981-3989.

Li, Q. and Z. Zhang [2010]. "*Dynamic Response of Pile in Saturated Porous Medium Considering Radial Heterogeneity by Pile Driving*", Soil Dyn. and Earthquake Engrg., Vol., 13, pp. 1-16.

Chai, H.Y., K.K. Phoon, C.F. Wei and Y.F. Lu [2011], "*Analysis of effects of active sources on observed phase velocity based on the thin layer method*", J. Appl. Geophy., Vol., 73, pp. 49–58.

Dominguez, J [1993], "*Boundary elements in dynamics*", Computational Mechanics Publications, Southampton, ISBN = 0-444-88820-9.

Liingaard, L.I.M. and L. Andersen [2007], *Impedance of flexible suction caissons*, Earthquake Engrg. and Struct. Dyn., Vol. 36, 2249-2271.

Prakash, S. and V. K. Puri [2006], "*Foundations for vibrating machines*" SERC J. of Struct. Engrg., Vol., 33(1), pp. 13-29.